Check for updates

Optimization of electron distribution by sulfidation: constructing a 1D S-Co₃O₄/ZnIn₂S₄ heterojunction for efficient visible-light-driven hydrogen evolution catalysis†

Hao Ji,[a] Zelin Li,[a] Zhenyi Xu,[b] Lingmin Yao, [ID] *[a] Rui Tong [ID] *[b] and Shan Zhang[a]

Developing an efficient visible-light-responsive catalyst for the hydrogen evolution reaction (HER) is essential for addressing energy scarcity and environmental pollution. In this study, one-dimensional Co_3O_4 (CO) nanoparticles were synthesized *via* electrospinning and subsequently sulfurized using a low-temperature solvothermal method. These sulfurized one-dimensional CO nanoparticles were then combined with two-dimensional sheet-like $ZnIn_2S_4$ (ZIS) to form a p–n heterojunction composite semiconductor photocatalyst (SCO/ZIS). The one-dimensional CO nanoparticles obtained through electrospinning significantly enhance the catalytic activity and efficiency, while sulfurization further improves their electronic structure and surface properties. The built-in electric field at the p–n heterojunction interface between n-type ZIS and p-type SCO effectively inhibits the recombination of photogenerated electron–hole pairs while facilitating electron transfer. Additionally, the incorporation of one-dimensional SCO into sheet-like ZIS prevents ZIS stacking, improving sunlight utilization and substantially enhancing photocatalytic HER performance. Our results demonstrate that SCO/ZIS achieves a superior HER rate of 4300.3 $\mu mol\ g^{-1}\ h^{-1}$ under visible light, which is 7.45 times higher than that of pristine ZIS, while also exhibiting excellent photocatalytic stability.

1. Introduction

Amid the global energy crisis and environmental pollution, hydrogen, as a renewable and clean energy source, is regarded as a promising solution to these challenges.[1–4] Photocatalytic hydrogen production technology is a promising approach for efficiently utilizing solar energy.[5–9] Since the discovery by Fujishima and Honda that titanium dioxide can split water,[10] A variety of photocatalysts have been developed, including metal sulfides, metal oxides, nitrogen oxides, organic polymers, and more.[11] But most metal oxides, due to the occupation of the O 2p orbital in the valence band, can only respond to ultraviolet (UV) light.[12,13] The development of semiconductor photocatalysts responsive to visible light becomes crucial for enhancing the utilization efficiency of solar radiation.[14] Metal sulfides, with appropriate band gaps, can respond to visible light, thereby increasing the efficiency of light utilization. This renders metal sulfide photocatalysts highly promising for

a more extensive range of applications in utilizing solar energy for hydrogen production.[15]

Among metal sulfides, zinc indium sulfide (ZIS) is an n-type semiconductor with a tunable bandgap ranging from 2.06 to 2.85 eV,[16] rendering it suitable for photocatalytic HER. The overlap of different atomic layers of S, Zn, and In can create an empty layer between two adjacent S layers, facilitating the capture of photogenerated electrons and achieving effective charge separation.[17] However, akin to many sulfide semiconductor photocatalysts, ZIS suffers from a significant drawback such as rapid recombination of photogenerated electron–hole pairs, resulting in diminished photocatalytic activity.[18–20] To enhance the photocatalytic performance of ZIS, various modulation strategies has been proposed, including morphology and structure control, vacancy and doping engineering, as well as the design and preparation of ZIS-based composite materials.[11,21–23] Gou *et al.*[24] used pyridine as a solvent and synthesized one-dimensional ZIS nanotubes and nanoribbons through a simple solvothermal method. The resulting nanomaterials exhibit strong absorption capabilities across a wide spectrum range.

In transition metal-based materials, cobalt-based compounds exhibit superior redox performance, with advantages such as low cost, ease of synthesis, and environmental friendliness.[25,26] Among them, Co_3O_4 is a p-type semiconductor

[a]School of Physics and Materials Science, Guangzhou University, Guangzhou, 510006, PR China. E-mail: lingminyao@gzhu.edu.cn

[b]Hubei Key Laboratory of Energy Storage and Power Battery, School of Optoelectronic Engineering, School of New Energy, Hubei University of Automotive Technology, Shiyan, 442002, PR China. E-mail: ruitong@huat.edu.cn

† Electronic supplementary information (ESI) available. See DOI: https://doi.org/10.1039/d5ra02995c

with excellent photothermal effects and stability. Constructing a p–n type heterojunction with n-type semiconductor photocatalysts can significantly improve its photocatalytic performance.[27,28] Shi *et al.*[29] synthesized shell-shaped composite material $Co_3O_4@ZIS$ by low-temperature solvothermal method, exhibiting a HER rate of 9.8 mmol g^{-1} h^{-1} under real sunlight. Zhang *et al.*[30] grew ultra-thin two-dimensional ZIS nanosheets on hollow Co_3O_4 nanotubes. This design prevents the aggregation of ZIS and achieves a high photocatalytic HER rate of 3.8 mmol g^{-1} h^{-1}. Designing heterostructures can optimize the electron distribution between different active materials, further enhancing the photocatalytic performances. By sulfiding Co_3O_4, regulating electronic structure can further enhance the catalyst's conductivity and catalytic performance. The combination of Co_3O_4 with metal sulfides to build composite photocatalysts is an effective strategy to boost photocatalytic activity.[26,31–35]

In this work, we utilized the electrospinning strategy to synthesize the C_3O_4 precursor, then air annealing and hydrothermal method to obtain one-dimensional sulfurized C_3O_4 (S-Co_3O_4), finally combining the S-Co_3O_4 with two-dimensional sheet-like ZIS to prepare p–n type heterojunction composite SCO/ZIS photocatalyst. Since Co_3O_4 and ZIS are p-type and n-type semiconductors, the p–n type heterojunction formed at the interface of the composite photocatalyst generates an internal electric field, suppressing the recombination of photoinduced carriers and facilitating rapid electron transfer. This enhancement ultimately improves the photocatalytic HER properties. The one-dimensional S-Co_3O_4 embedded on the surface of sheet-like ZIS effectively prevents the stacking of ZIS, thereby increasing the utilization efficiency of visible light. The synthesized SCO/ZIS exhibits an impressive HER rate of 4300.3 µmol g^{-1} h^{-1} under visible light, which is 7.45 times higher than that of pure ZIS.

2. Materials and characterizations

2.1. Materials

The chemicals utilized in this study include cobalt nitrate hexahydrate ($Co(NO_3)_2 \cdot 6H_2O$, Aladdin, 99%), 2-methylimidazole (Macklin, 98%), methanol (Aladdin, ≥99.5%), cetyl trimethylammonium bromide (CTAB, Aladdin, ≥99%), polyacrylonitrile (PAN, MW = 150 000, Aladdin), *N,N*-dimethylformamide (DMF, Macklin, ≥99.9%), thioacetamide (TAA, Aladdin, ≥98%), zinc acetate dihydrate ($Zn(OCOCH_3)_2 \cdot 2H_2O$, Aladdin, ≥99%), indium trichloride tetrahydrate ($InCl_3 \cdot 4H_2O$, Aladdin, 98%), glacial acetic acid (Aladdin, 98%), glycerin (GL, Aladdin, ≥99%), triethanolamine (TEOA, Aladdin, ≥99.5%).

2.2. Fabricating of photocatalysts

The preparation process of the composite photocatalyst is presented in Fig. 1.

2.2.1 Preparation of ZIF-67. Dissolve 2.9 g of $Co(NO_3)_2 \cdot 6H_2O$ in 70 ml of methanol solution, then add 32 mg of CTAB to form solution A. Dissolve 6.5 g of 2-methylimidazole in 70 ml of methanol as solution B. Then, solution B and B were mixed

together at 20 °C for 24 h. Subsequently, washed with ethanol and dried in vacuum to obtain ZIF-67.

2.2.2 Preparation of 1D S-Co_3O_4. Firstly, dissolve 500 mg of ZIF-67 and 500 mg of PAN (MW = 150 000) in 7 ml of DMF solution, mix and stir overnight to obtain a precursor solution. Load 7 ml of the precursor solution into a 20 ml syringe, pump the solution at a rate of 1 ml h^{-1}, and apply a voltage of 17 kV for electrospinning to obtain 1D ZIF-67 nanofibers. Secondly, after drying overnight at 60 °C, calcine the nanofibers at 600 °C in air for 4 hours to obtain 1D Co_3O_4. Finally,60 mg of one-dimensional Co_3O_4, 100 mg of thioacetamide (TAA), and 30 ml of ethanol were placed in a Teflon-lined stainless-steel autoclave and heated at 120 °C for 4 hours. Subsequently, washed with ethanol and dried in vacuum to obtain 1D S-Co_3O_4. For convenience in the following text, S-CO_3O_4 will be abbreviated as SCO.

2.2.3 Preparation of 1D S-Co_3O_4/$ZnIn_2S_4$. 221 mg $Zn(OCOCH_3)_2 \cdot 2H_2O$, 293 mg $InCl_3 \cdot 4H_2O$, and 304 mg TAA were added into 8 mL glycerol with 32 ml deionized water (pH = 2.5). After complete mixing, add an appropriate amount of 1D S-Co_3O_4. Then the aboved well-mixed solution was stirred in oil bath for 4 h at 80 °C. Subsequently, washed with ethanol and dried in vacuum to obtain 1D S-Co_3O_4/$ZnIn_2S_4$. In this work, the samples containing different mass ratios of 1D S-Co_3O_4/$ZnIn_2S_4$ are designated as ZIS-X (where X represents the mass ratio of 1D S-Co_3O_4). The original ZIS was prepared using the same method only without adding S-Co_3O_4.

2.3. Characterization

The structural characterization of the prepared photocatalysts was performed using X-ray diffraction (XRD, PW3040/60, PANalytical, Netherlands). The micromorphology and lattice fringes were analyzed using field emission scanning electron microscopy (SEM, JSM-7001F, JEOL) and transmission electron microscopy (TEM, Talos-F200S, FEI). Photoluminescence (PL) and time-resolved photoluminescence (TRPL) spectra were obtained using a fluorescence spectrometer (FS5, Edinburgh Instruments) at an excitation wavelength of 375 nm. The X-ray photoelectron spectroscopy (XPS) was used to test the surface composition and valence structure. Optical absorption characteristics were evaluated with a UV-vis spectrophotometer (UV-3600Plus, Shimadzu). To analyze transient free radicals in both raw and composite samples, electron spin resonance (ESR) measurements were carried out with a Bruker EMXplus-6/1 spectrometer (Germany). DMPO (5,5-dimethyl-1-pyrroline-*N*-oxide) served as a spin-trapping agent, and superoxide radical generation was quantitatively studied under both dark and illuminated conditions for three minutes.

2.4. Photoelectrochemical measurement

Photocurrent response tests, Mott–Schottky analysis, electrochemical impedance spectroscopy (EIS), and linear sweep voltammetry (LSV) were performed using a three-electrode setup. The working electrode was prepared as follow: 10 mg photocatalysts, 200 µL ethanol and 20 µL Nafion solution were ultrasound to obtain a uniform suspension. This dispersion was
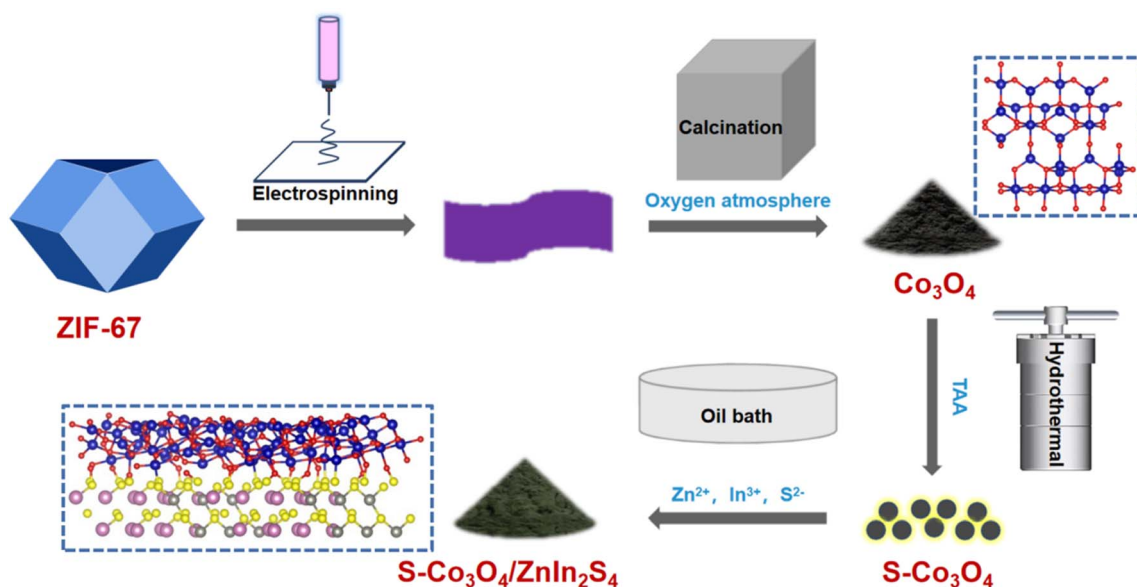
Fig. 1 Schematic of synthesis of S-Co$_3$O$_4$/ZnIn$_2$S$_4$.

then coated onto a cleaned indium tin oxide (ITO)-coated glass substrate. ITO glasses were cleaned several times *via* ultra-sonication with deionized water, ethanol and acetone. A 300 W Xe lamp equipped with a UV cutoff filter ($\lambda > 420$ nm) was used as the light source. A 0.5 M Na$_2$SO$_4$ solution served as the electrolyte.

2.5. Photocatalytic H$_2$ evolution performance

We adopted the Labsolar-6A system (PerfectLight) to monitor photocatalytic HER. 10 mg of photocatalyst was put into a 100 ml solution consisting of 90 ml water and 10 ml TEOA (triethanolamine), followed by 30 minutes of sonication to ensure thorough mixing. A 300 W Xe lamp ($\lambda > 420$ nm) served as the light source. Prior to illumination, the system was vac-uumed to remove impurities. The reaction temperature is 5 to 20 °C. The hydrogen production were recorded using a gas chromatograph (GC9790II, FuLi). We calculated the apparent quantum yield (AQY) using following formula:

$$AQY(\%) = \frac{(\text{number of evolved } H_2 \text{ molecules} \times 2)}{(\text{number of incident photos})} \times 100\%$$

3. Results and discussion

We adopted XRD to analyze the crystalline phase and structure. As shown in Fig. 2(a), the peaks at 21.58°, 27.69°, 47.17°, and 52.44°, matching to the (006), (102), (110), and (116) crystal planes of hexagonal phase of ZIS. These data are consistent with the standard PDF card in Fig. 2(b) (JCPDS No. 65-2023). SCO shows prominent diffraction peaks at 31.16°, 36.84°, 44.8°, 59.34°, and 65.22° in accordance with the (220), (311), (400), (511), and (440) crystal planes in Fig. 2(b) (JCPDS No. 78-1970). Due to the weak intensity of the diffraction peaks and the overlap of characteristic peaks with Co$_3$O$_4$, it is difficult to identify CoS in the diffraction pattern. From the diffraction patterns, it can be observed that with the increase in SCO
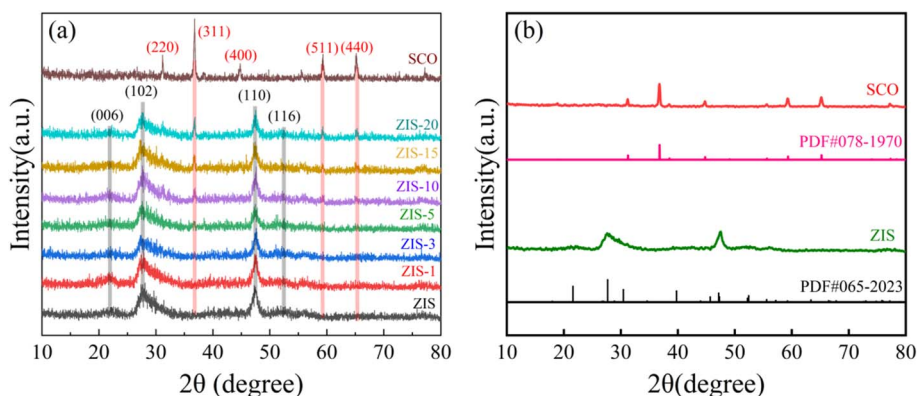

Fig. 2 (a) XRD patterns, (b) comparison chart of the sample and the standard card.
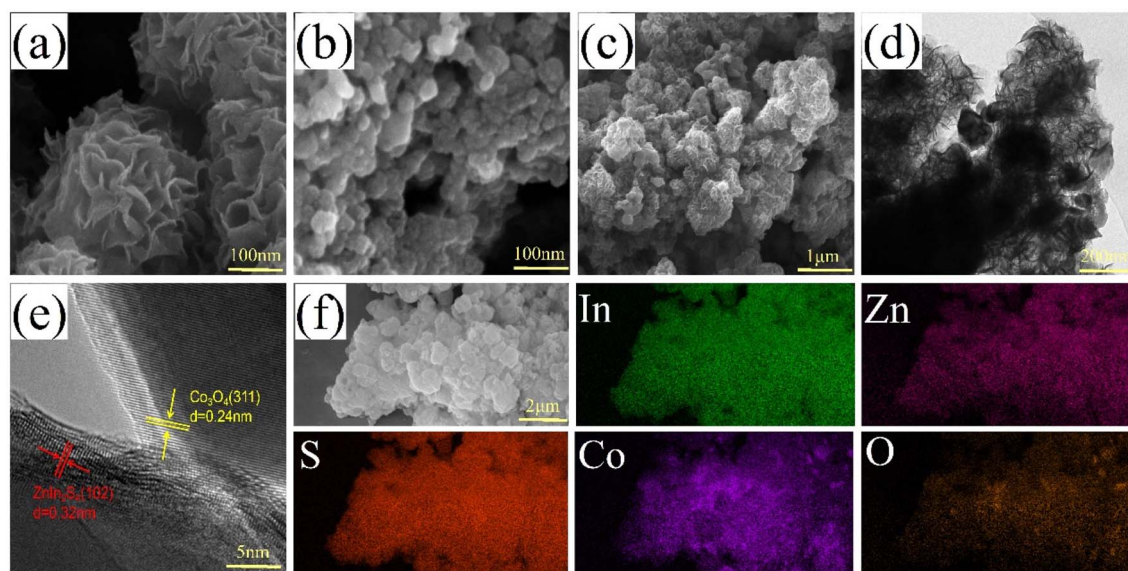
Fig. 3 SEM images of (a) ZIS, (b) 1D SCO, and (c) ZIS-15; TEM images of ZIS-15 (d and e); EDX mappings of ZIS-15 (f).

content, the intensity of diffraction peaks at the (311) (36.84°) and (440) (65.22°) planes of ZIS-X gradually increases, indicating the successful synthesis of the $ZnIn_2S_4/S-Co_3O_4$ photocatalyst.

The morphology and microstructure of the samples were analyzed using SEM and TEM. Fig. 3(a) shows the original synthesized ZIS sample, which is a stacked layered nanosheet structure. Fig. 3(b) show the 1D SCO nanoparticles obtained after calcination following electrospinning. Fig. 3(c) is ZIS-15, where 1D SCO nanoparticles can be seen adhering to the flaky ZIS, forming a tightly integrated heterojunction interface, enhancing the dispersion of the nanosheets. Further observation of the TEM image of ZIS-15 (Fig. 3(d)) reveals a good combination of 1D SCO nanoparticles with ZIS nanosheets. At the intersection points, there are small gaps and an uneven surface, which increases light reflection and scattering, thus improving light utilization efficiency. Fig. 3(e) shows two different lattices: the (102) plane of ZIS with a spacing of 0.21 nm and the (311) plane of CO with a lattice spacing of 0.24 nm. Elements In, Zn, S, Co, and O can all be mapped on the EDX (Fig. 3(f)), presenting a uniformly distributed state.

The surface chemical composition of ZIS, ZIS-15, 1D SCO were analyzed by XPS. As shown in Fig. 4(a), Zn, In, S, Co, O could be detected. Compared to the original ZIS, there are subtle changes in the peaks of ZIS-15. These changes are caused by the strong interaction within the heterostructure formed by SCO and ZIS. The two peaks of Zn 2p at 1022.1 and 1045.1 eV correspond to Zn $2p_{3/2}$ and Zn $2p_{1/2}$, respectively (Fig. 4(b)).[36] The two peaks of In 3d at 445.24 and 452.49 eV correspond to In $3d_{5/2}$ and In $2d_{3/2}$, respectively (Fig. 4(c)).[37,38] The two peaks of S 2p at 161.41 and 162.70 eV correspond to S $2p_{3/2}$ and S $2p_{1/2}$, respectively (Fig. 4(d)).[39] The element S can be detected in SCO, and the peak at 161.63 eV corresponds to the metal sulfide bond, indicating the presence of CoS in SCO and the successful construction of the CoS/Co_3O_4 heterostructure. The spectrum of

Co 2p can be decomposed into four characteristic peaks (Fig. 4(e)). The peaks at 779.86 and 794.64 eV belong to Co^{3+} $2p_{3/2}$ and Co^{3+} $2p_{1/2}$,[40] and the peaks at 781.90 and 796.26 eV belong to Co^{2+} $2p_{3/2}$ and Co^{2+} $2p_{1/2}$.[41] This indicates the presence of Co in both divalent and trivalent states in the SCO sample. Due to the low content of SCO in the ZIS-15 sample and the close combination of the flaky stacked ZIS with SCO, the Co diffraction peak observed on ZIS-15 is very weak. The O 1 s spectrum can be deconvoluted into three characteristic peaks, with the peak at 530.24 eV attributed to lattice oxygen, while the other two peaks correspond to surface-adsorbed oxygen (Fig. 4(f)).[42] The XPS analysis presented in Fig. 4(e) and (f) reveals that both the Co 2p and O 1s in ZIS-15 sample move toward lower binding energies in comparision with pure SCO, which indicates an increase in the electron density of SCO. As shown in Fig. 4(b)–(d), compared with ZIS, the Zn 2p, In 3d, and S 2p of ZIS-15 sample shift to higher energy, which indicates a decrease in the electron density of ZIS. This suggests that the electrons in ZIS migrates to SCO. Thus, an internal electric field is established between ZIS and SCO.[43] Such modifications facilitate the migration of charge carriers, ultimately leading to an enhancement in photocatalytic performance.[44]

To further study the influence of SCO on the charge transfer efficiency of ZIS, transient photocurrent response tests and electrochemical impedance spectroscopy were conducted using an electrochemical workstation. Fig. 5(a) shows the transient photocurrent response graphs of the pristine ZIS sample and the composite sample ZIS-15. The graph clearly shows that the photocurrent density of the composite sample ZIS-15 is markedly higher than that of ZIS. This suggests that integrating ZIS with SCO enhances the photocurrent response, leading to improved electron transfer efficiency.[45] The EIS test was used to study the electron transfer efficiency (Fig. 5(b)). ZIS-15 exhibits a smaller Nyquist semicircle than ZIS, suggesting reduced resistance to electron migration after ZIS is combined with
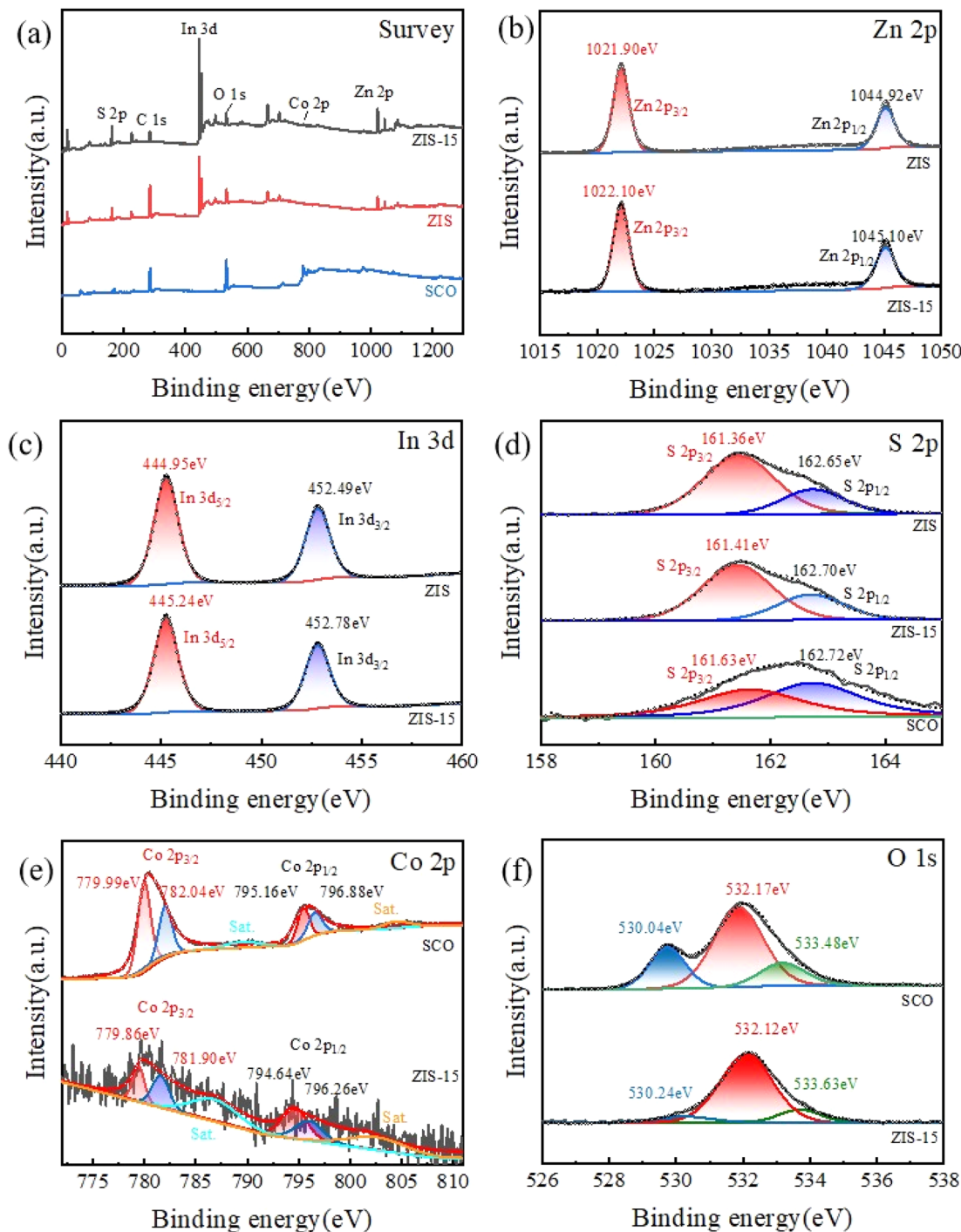
Fig. 4 XPS spectrum of ZIS, ZIS-15, and SCO. (a) Survey, (b) Zn 2p, (c) In 3d, (d) S 2p, (e) Co 2p, (f) O 1s.

SCO.[46] Fig. 5(c) exhibits the ESR spectra of the sample with DMPO as a radical scavenger, detecting superoxide radicals in the original and composite samples under dark and light conditions. There were no characteristic peaks of ·O_2^- radicals in the spectra of samples under dark conditions. After irradiating the composite sample with light for three minutes, four similar characteristic peaks of superoxide radicals were observed, exhibiting a typical 1 : 2 : 2 : 1 peak intensity curve which was consistent with previous reports. This indicates an increase in the number of radicals in the sample under illumination. The intensity of ZIS-15 was significantly higher than ZIS, indicating that ZIS-15 has a higher efficiency compared to ZIS.

Fig. 5(d) exhibits the PL spectra of ZIS and ZIS-15, where ZIS-15 displays significantly lower PL intensity than the pure ZIS. The decreased emission intensity shows a lower carriers
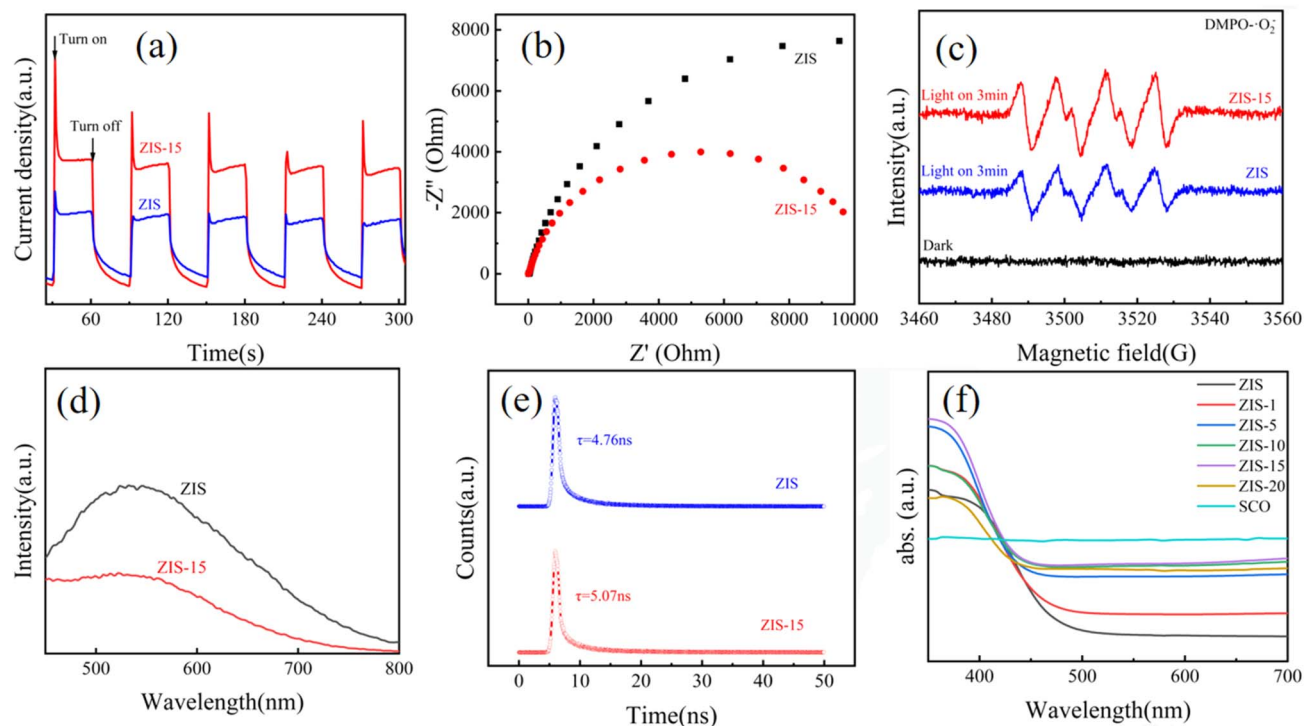
Fig. 5 Photocurrent response graph (a), nyquist impedance spectra (b) of ZIS and ZIS-15; (c) ESR spectra of ZIS and ZIS-15 under dark and illuminated conditions; PL (d) and TRPL (e) of ZIS and ZIS-15; (f) UV spectra.
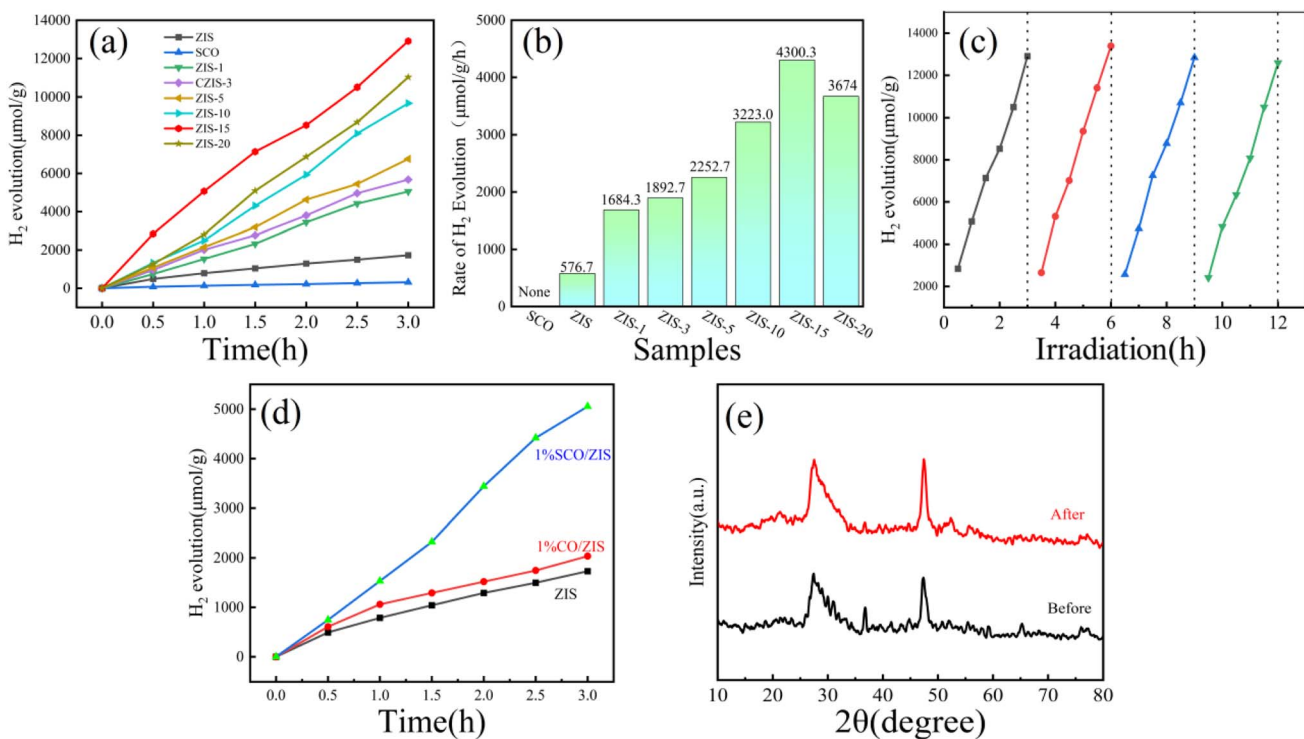

Fig. 6 (a) Hydrogen evolution stability diagram of ZIS-X; (b) hydrogen evolution performance diagram of ZIS-X; (c) 12 hours long-term cycling experiment diagram of ZIS-15; (d) comparison of hydrogen evolution performance between ZIS, ZIS with 1% Co_3O_4 doping, and ZIS with 1% S-Co_3O_4 doping; (e) XRD diffraction patterns of ZIS before and after reaction.

recombination rate, effectively suppressing the recombination of photogenerated electrons. As shown in Fig. 5(e), the average charge lifetime of ZIS is 4.76 ns, whereas that of ZIS-15 extends to 5.07 ns. A longer charge lifetime indicates an increased opportunity for charges to engage in surface reactions.[47,48] All these results demonstrate that after combining ZIS with SCO, the rate of photocurrent migration significantly increases, the recombination of photogenerated electrons is inhibited. The absorption spectra were obtained in the range of 300 nm to 700 nm in the experiment. As shown in Fig. 5(f), the prepared composite ZIS-X samples exhibited good light absorption capability in the range of 300 to 500 nm, showing an absorption edge at around 460 nm. The SCO sample demonstrated uniform light absorption across all wavelengths. With an increase in the SCO mass ratio, the light absorption capability of the composite samples in the visible light region gradually strengthened. Among them, ZIS-15 showed the most excellent light absorption capability.

Under visible light irradiation ($\lambda > 420$ nm), triethanolamine (TEOA) was used as a sacrificial agent to analyze the HER performance of the SCO/ZIS composite photocatalysts. The tests were conducted over a period of 3 hours. Fig. 6(a) presents the sustained hydrogen production of ZIS with varying SCO mass ratios, highlighting the excellent stability. Fig. 6(b) shows the HER performances. The original SCO sample exhibited almost no hydrogen evolution activity, while the original ZIS sample

had a HER rate of only 576.7 μmol g^{-1} h^{-1}. As the mass ratio of SCO increases, the HER performance of the composite photocatalyst shows a significant upward trend. When the SCO mass ratio reaches 15%, the composite achieves its highest HER rate of 4300.3 μmol g^{-1} h^{-1}, which is 7.45 times greater than that of the original ZIS. This improvement is attributed to the heterojunction formed between SCO and ZIS, which suppresses the rapid carriers recombination and significantly enhances the carriers migration rate, thereby greatly accelerating the photocatalytic hydrogen evolution process. However, further increase in the amount of SCO leads to a decline in hydrogen evolution performance, indicating that excessive SCO can affect the photocatalytic activity of ZIS. Excessive addition reduces the concentration of ZIS, the primary catalyst, and can also hinder light irradiation, lowering the utilization rate of light by the main catalyst. Therefore, the optimal loading amount of SCO is 15 wt%. The AQE at 420 nm is 18.02%. Subsequent experiments were conducted four times continuously to analyze the stability of the composite photocatalyst in hydrogen evolution. After a long cycle of 12 hours (Fig. 6(c)), the performance of SCO/ZIS remained nearly unchanged and consistently stable. In Fig. 6(d), a comparative experiment was performed on the HER performance of ZIS combined separately with 1% mass ratio Co$_3$O$_4$ and 1% mass ratio SCO. It was observed that the ZIS sample combined only with CO showed a small improvement in hydrogen evolution performance compared to ZIS alone, while
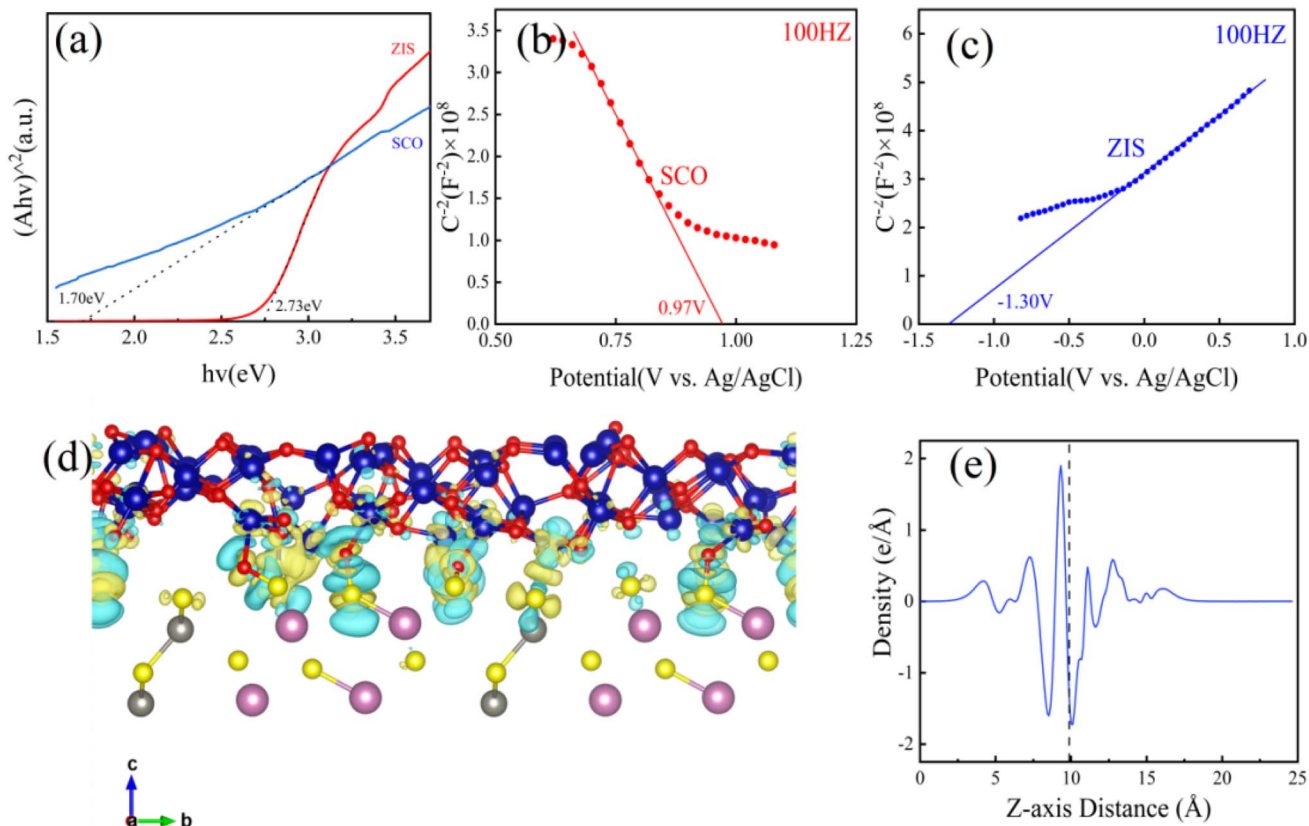

Fig. 7 (a) Tauc plot of ZIS and SCO; Mott–Schottky plots for (b) SCO and (c) ZIS; charge density difference (d) and interfacial charge transfer (e) along the Z-direction of SCO/ZIS.

the sample combined with SCO exhibited a significant enhancement in hydrogen evolution performance. By comparing the XRD spectra after the reaction (Fig. 6(e)), it was observed that there were no significant changes. As shown in Table S1,† this is a comparison of the activity of catalysts for some similar systems.

The band gap of the composite photocatalyst was determined using the Kubelka–Munk equation[49] ($\alpha h\nu = A(h\nu - E_g)^{1/2}$) to analyze its band structure. The calculated band gaps of original ZIS and SCO are 2.73 eV and 1.70 eV (Fig. 7(a)). Fig. 7(b) and (c) show the Mott–Schottky plots measured at 100 Hz, where the slope of the tangent line for ZIS is positive, suggesting it an n-type semiconductor, and the slope for SCO is negative, indicating a p-type semiconductor.[50–53] The flat band potentials (V_{FB}) of ZIS and SCO are −1.30 V and 0.97 V, respectively. The conduction band (CB) of ZIS is −1.5 eV, and the valence band (VB) of SCO is 1.17 eV. According to the formula $E_{VB} = E_{CB} + E_g$,[54] the valence band of ZIS is calculated to be 1.23 eV (as shown in Fig. S1,† it is consistent with the results measured by XPS valence band spectrum), and the conduction band of SCO is 0.53 eV. To better clarify the interfacial charge transfer between SCO and ZIS, DFT was employed to study the electron density distribution at the interface. As depicted in Fig. 7(d) and (e), the yellow and blue regions represent charge accumulation and depletion, respectively. It can be observed that charge redistribution occurs at the interface, leading to the formation of an internal electric field, which effectively facilitates the separation of photogenerated electron–hole pairs.[55]

Fig. 8(a) illustrates the band structures of ZIS and SCO. When the composite is formed, a bandgap shift takes place, facilitating electron transfer from SCO to ZIS. This leads to a decrease in the Fermi level of ZIS until a new equilibrium is reached. Concurrently, a new electric field is formed at the interface of the p–n heterojunction, as depicted in Fig. 8(b). Fig. 8(c) depicts a simplified schematic of the hydrogen evolution process. Upon excitation by light radiation, electrons on the valence band swiftly migrate to the conduction band and then combine with free hydrogen ions in water, producing hydrogen gas. In the absence of SCO composite, photogenerated electrons exhibit rapid recombination with holes, resulting in poor hydrogen evolution performance of the sample. However, after composite formation with SCO, separated photogenerated electrons swiftly transfer from the CB of SCO to CB of ZIS, facilitating hydrogen evolution. Meanwhile, separated holes can rapidly migrate from the valence band of ZIS to valence band of SCO, where they react with and are consumed by the sacrificial agent triethanolamine (TEOA). Furthermore, the internal electric field generated at the p–n
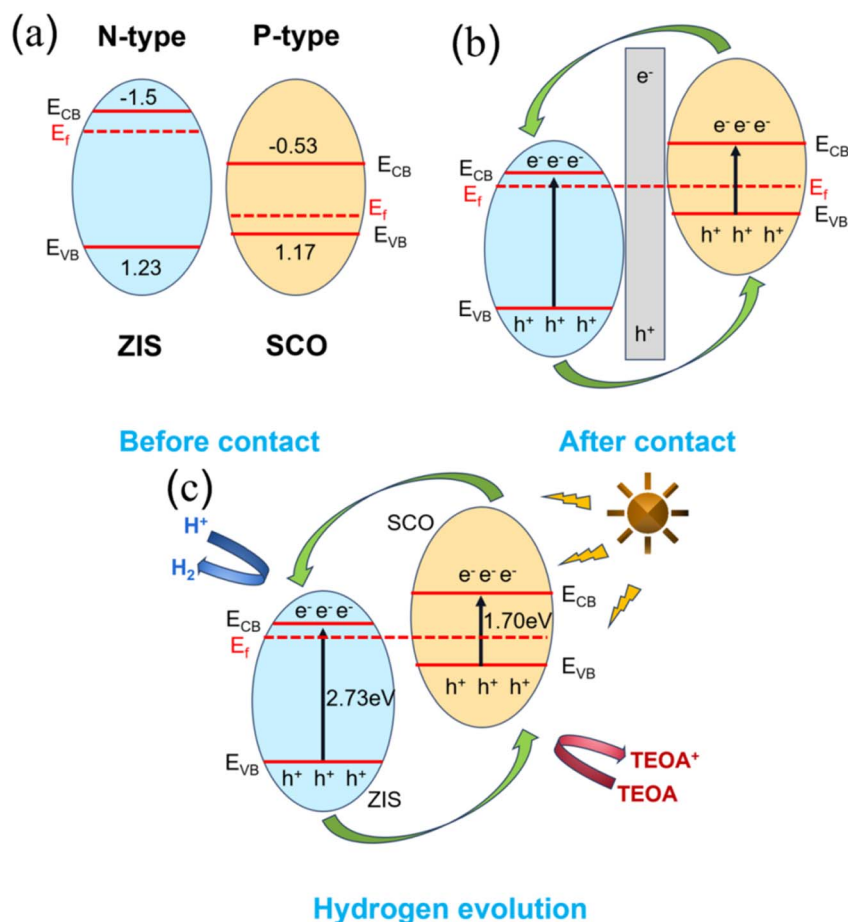

Fig. 8 The potential mechanism of photocatalytic hydrogen evolution.

heterojunction enhances the separation and migration of electron–hole pairs, thereby boosting the photocatalytic hydrogen evolution performance. Furthermore, the uneven surface of the S-Co_3O_4/$ZnIn_2S_4$ composite photocatalyst provides a favorable environment for light scattering and reflection, significantly increasing light utilization. Due to these positive effects, S-Co_3O_4/$ZnIn_2S_4$ exhibits excellent photocatalytic hydrogen evolution performance.

4. Conclusions

We employed the electrospinning method to synthesize one-dimensional CO nanoparticles, which were subsequently sulfided *via* a hydrothermal process. Finally, a high-performance p–n heterojunction photocatalyst, SCO/ZIS, was successfully fabricated using a low-temperature oil bath method. The incorporation of an optimal amount of SCO (15% by mass) significantly enhanced the photocatalytic HER property of ZIS. The p–n heterojunction formed within the composite photocatalyst efficiently facilitated the separation and migration of photogenerated electron–hole pairs, directing electrons and holes into their respective conduction and valence bands. This process effectively suppressed electron–hole recombination. Under visible light irradiation, the composite achieved a hydrogen evolution rate of 4300.3 μmol g^{-1} h^{-1}, which is 7.45 times higher than that of pristine ZIS. Moreover, the composite photocatalyst demonstrated excellent stability over prolonged catalytic cycles. This study offers a viable approach and valuable insights for designing p–n heterojunction photocatalysts by integrating transition metal-based materials with semiconductors.

Data availability

Data will be made available on request.

Conflicts of interest

There are no conflicts of interest to declare.

Acknowledgements

References

1 R. Tong, K. W. Ng, X. A. Wang, S. P. Wang, X. S. Wang and H. Pan, *J. Mater. Chem. A*, 2020, **8**, 23202–23230.
2 M.-Y. Qi, M. Conte, M. Anpo, Z.-R. Tang and Y.-J. Xu, *Chem. Rev.*, 2021, **121**, 13051–13085.
3 R. Tong, M. Xu, H. M. Huang, C. K. Zhang, Y. A. Ma, X. N. Wang, X. S. Hu, Y. J. Qu, S. P. Wang and H. Pan, *ACS Appl. Energy Mater.*, 2022, **5**, 440–448.
4 Y. X. Chen, J. Meng, M. Xu, L. L. Qiao, D. Liu, Y. C. Kong, X. S. Hu, Q. J. Liu, M. P. Chen, S. Lyu, R. Tong and H. Pan, *Adv. Funct. Mater.*, 2025, **35**, 2413474.
5 Y. Liu, X. Hao, H. Hu and Z. Jin, *Acta Phys.-Chim. Sin.*, 2021, **37**, 2008030.
6 S. Wang, P. Liu, C. Meng, Y. Wang, L. Zhang, L. Pan, Z. Yin, N. Tang and J.-J. Zou, *J. Catal.*, 2022, **408**, 196–205.
7 Y.-C. Zhang, N. Afzal, L. Pan, X. Zhang and J.-J. Zou, *Adv. Sci.*, 2019, **6**, 1900053.
8 R. Zhang, Y.-C. Zhang, L. Pan, G.-Q. Shen, N. Mahmood, Y.-H. Ma, Y. Shi, W. Jia, L. Wang, X. Zhang, W. Xu and J.-J. Zou, *ACS Catal.*, 2018, **8**, 3803.
9 C. P. Xu, P. R. Anusuyadevi, C. Aymonier, R. Luque and S. Marre, *Chem. Soc. Rev.*, 2019, **48**, 3868–3902.
10 A. Fujishima and K. Honda, *Nature*, 1972, **238**, 37–38.
11 R. J. Yang, L. Mei, Y. Y. Fan, Q. Y. Zhang, R. S. Zhu, R. Amal, Z. Y. Yin and Z. Y. Zeng, *Small Methods*, 2021, **5**, 2100887.
12 W. Zhang, H. He, H. Li, L. Duan, L. Zu, Y. Zhai, W. Li, L. Wang, H. Fu and D. Zhao, *Adv. Energy Mater.*, 2021, **11**, 2003303.
13 M. M. Gao, L. L. Zhu, C. K. Peh and G. W. Ho, *Energy Environ. Sci.*, 2019, **12**, 841–864.
14 Q. H. Zhu, Q. Xu, M. M. Du, X. F. Zeng, G. F. Zhong, B. C. Qiu and J. L. Zhang, *Adv. Mater.*, 2022, **34**, 2202929.
15 G. Radovsky, R. Popovitz-Biro, M. Staiger, K. Gartsman, C. Thomsen, T. Lorenz, G. Seifert and R. Tenne, *Angew. Chem., Int. Ed.*, 2011, **50**, 12316–12320.
16 R. Xiao, C. Zhao, Z. Zou, Z. Chen, L. Tian, H. Xu, H. Tang, Q. Liu, Z. Lin and X. Yang, *Appl. Catal., B*, 2020, **268**, 118382.
17 H. Song, S. Liu, Z. Sun, Y. Han, J. Xu, Y. Xu, J. Wu, H. Meng, X. Xu, T. Sun and X. Zhang, *Sep. Purif. Technol.*, 2021, **275**, 120585.
18 X. Feng, H. Shang, J. Zhou, D. Wang, B. Zhang, X. Gao and Y. Zhao, *Chem. Eng. J.*, 2023, **457**, 141192.
19 Z. Q. Xiang, H. J. Guan, B. Zhang and Y. F. Zhao, *J. Am. Ceram. Soc.*, 2021, **104**, 504–513.
20 G. P. Zhang, H. Wu, D. Y. Chen, N. J. Li, Q. F. Xu, H. Li, J. H. He and J. M. Lu, *Green Energy Environ.*, 2022, **7**, 176–204.
21 Q. Zhang, X. Wang, J. Zhang, L. Li, H. Gu and W.-L. Dai, *J. Colloid Interface Sci.*, 2021, **590**, 632–640.
22 Z.-H. Xue, D. Luan, H. Zhang and X. W. Lou, *Joule*, 2022, **6**, 92–133.
23 L. Shi, P. Q. Yin and Y. M. Dai, *Langmuir*, 2013, **29**, 12818–12822.
24 X. Gou, F. Cheng, Y. Shi, L. Zhang, S. Peng, J. Chen and P. Shen, *J. Am. Chem. Soc.*, 2006, **128**, 7222–7229.

25 Y. Fang, X. Li, F. Li, X. Lin, M. Tian, X. Long, X. An, Y. Fu, J. Jin and J. Ma, *J. Power Sources*, 2016, **326**, 50–59.

26 W. Zhang, W. Chen, Q. Xiao, L. Yu, C. Huang, G. Lu, A. W. Morawski and Y. Yu, *Appl. Catal., B*, 2020, **268**, 118449.

27 S. Jian, X. Ma, Q. Wang, J. Wu, Y. Wang, S. Jiang, W. Xu and W. Yang, *Vacuum*, 2021, **184**, 109879.

28 W. Cao, W. Wang, H. Shi, J. Wang, M. Cao, Y. Liang and M. Zhu, *Nano Res.*, 2018, **11**, 1437–1446.

29 Y. Shi, L. Li, Z. Xu, F. Guo and W. Shi, *Chem. Eng. J.*, 2023, 459.

30 Y. Zhang, D. Chen, N. Li, Q. Xu, H. Li and J. Lu, *Appl. Surf. Sci.*, 2023, **610**, 155272.

31 H. Xu, H. Shang, C. Wang, L. Jin, C. Chen, C. Wang and Y. Du, *Appl. Catal., B*, 2020, **265**, 118605.

32 J. Lin, H. Wang, Y. Yan, J. Cao, C. Qu, X. Zheng, J. Feng and J. Qi, *J. Power Sources*, 2020, **445**, 227294.

33 J. Yin, Y. Li, F. Lv, M. Lu, K. Sun, W. Wang, L. Wang, F. Cheng, Y. Li, P. Xi and S. Guo, *Adv. Mater.*, 2017, **29**, 1704681.

34 R. S. Devan, R. A. Patil, J. H. Lin and Y. R. Ma, *Adv. Funct. Mater.*, 2012, **22**, 3326–3370.

35 G. R. Yang, W. Yan, J. A. Wang and H. H. Yang, *Mater. Lett.*, 2014, **122**, 117–120.

36 H. H. Song, S. Y. Liu, Z. Q. Sun, Y. D. Han, J. L. Xu, Y. Xu, J. B. Wu, H. Meng, X. X. Xu, T. Sun and X. Zhang, *Sep. Purif. Technol.*, 2021, **275**, 119153.

37 Y. X. Shi, L. L. Li, Z. Xu, F. Guo and W. L. Shi, *Chem. Eng. J.*, 2023, 459.

38 J. Y. Chen, H. M. Zhang, P. R. Liu, Y. B. Li, X. L. Liu, G. Y. Li, P. K. Wong, T. C. An and H. J. Zhao, *Appl. Catal., B*, 2015, **168**, 266–273.

39 S. G. Meng, C. Chen, X. M. Gu, H. H. Wu, Q. Q. Meng, J. F. Zhang, S. F. Chen, X. L. Fu, D. Liu and W. W. Lei, *Appl. Catal., B*, 2021, **285**, 119789.

40 Z. Xunfu, L. Ziqing, P. Lanzhen, X. Minyi, X. Yuanxuan, L. Jin, N. Xiaomei, F. Xuliang, F. Huile and Z. Xiaosong, *Int. J. Hydrogen Energy*, 2025, **135**, 10–19.

41 J. Wu, Y. Dai, Z. J. Pan, D. X. Huo, T. Wang, H. P. Zhang, J. Hu and S. Yan, *Appl. Surf. Sci.*, 2020, **510**, 145529.

42 H. Li, F. Yue, C. Yang, P. Qiu, P. Xue, Q. Xu and J. D. Wang, *Ceram. Int.*, 2016, **42**, 3121–3129.

43 X. F. Zhou, Y. X. Xian, Z. Q. Li, C. Yujie, J. Luo, X. M. Ning, X. L. Fan, Y. M. Zhong and X. S. Zhou, *Sep. Purif. Technol.*, 2025, **357**, 12.

44 X. S. Zhou, J. B. Liang, L. M. Xu, S. Y. Wu, M. Y. Xie, Q. D. Liang, J. Luo, X. L. Fan, X. F. Zhou and X. Q. Zhou, *J. Colloid Interface Sci.*, 2025, **689**, 10.

45 H. Fan, Y. Jin, K. Liu and W. Liu, *Adv. Sci.*, 2022, **9**, 2104579.

46 K. Khan, L. Xu, M. Shi, J. Qu, X. Tao, Z. Feng, C. Li and R. Li, *Chin. J. Catal.*, 2021, **42**, 1004–1012.

47 W. Liu, Y. Wang, H. Huang, J. Wang, G. He, J. Feng, T. Yu, Z. Li and Z. Zou, *J. Am. Chem. Soc.*, 2023, **145**, 7181–7189.

48 S. Chen, J. Liao, Z. Zhou, S. Yang, Q. Gao, X. Cai, F. Peng, Y. Fang and S. Zhang, *Appl. Catal., B*, 2021, **291**, 120139.

49 A. A. Kokhanovsky, *J. Phys. D:Appl. Phys.*, 2007, **40**, 2210–2216.

50 M. Li, S. Zhang, L. Li, J. Han, X. Zhu, Q. Ge and H. Wang, *ACS Sustain. Chem. Eng.*, 2020, **8**, 11465–11476.

51 H. Gong, G. Wang, H. Li, Z. Jin and Q. Guo, *Int. J. Hydrogen Energy*, 2020, **45**, 26733–26745.

52 X. H. Ma, Y. N. Liu, Y. P. Wang and Z. L. Jin, *Int. J. Hydrogen Energy*, 2021, **46**, 33809–33822.

53 W. L. Shi, C. C. Hao, Y. M. Fu, F. Guo, Y. B. Tang and X. Yan, *Chem. Eng. J.*, 2022, **433**, 133741.

54 Z. Chen, F. Guo, H. Sun, Y. Shi and W. Shi, *J. Colloid Interface Sci.*, 2022, **607**, 1391–1401.

55 T. Li, N. Tsubaki and Z. L. Jin, *J. Mater. Sci. Technol.*, 2024, **169**, 82–104.